

Three-dimensional frequency-wavenumber method for efficient and high-quality volumetric ultrasound imaging

Huchang Guan(关虎昌), Chen Jiang(江晨), Kailiang Xu(许凯亮), and Dean Ta(他得安)
Citation: Chin. Phys. B, 2026, 35 (**7**): 074301. DOI: 10.1088/1674-1056/ae42b9
http://cpb.iphy.ac.cn; http://iopscience.iop.org/cpb

What follows is a list of articles you may be interested in

Lamb wave TDTE super-resolution imaging assisted by deep learning

Liu-Jia Sun(孙刘家), Qing-Bang Han(韩庆邦), and Qi-Lin Jin(靳琪琳)
Chin. Phys. B, 2025, 34 (**1**): 014301. DOI: 10.1088/1674-1056/ad886d

Deep learning for image reconstruction in thermoacoustic tomography

Qiwen Xu(徐启文), Zhu Zheng(郑铸), and Huabei Jiang(蒋华北)
Chin. Phys. B, 2022, 31 (**2**): 024302. DOI: 10.1088/1674-1056/ac0dab

Location of micro-cracks in plates using time reversed nonlinear Lamb waves

Yaoxin Liu(刘尧鑫), Aijun He(何爱军), Jiehui Liu(刘杰惠), Yiwei Mao(毛一葳), Xiaozhou Liu(刘晓宙)
Chin. Phys. B, 2020, 29 (**5**): 054301. DOI: 10.1088/1674-1056/ab81f7

Lamb waves topological imaging combining with Green's function retrieval theory to detect near filed defects in isotropic plates

Hui Zhang(张辉), Hai-Yan Zhang(张海燕), Meng-Yun Xu(徐梦云), Guo-Peng Fan(范国鹏), Wen-Fa Zhu(朱文发), Xiao-Dong Chai(柴晓冬)
Chin. Phys. B, 2019, 28 (**7**): 074301. DOI: 10.1088/1674-1056/28/7/074301

Three-dimensional frequency-wavenumber method for efficient and high-quality volumetric ultrasound imaging

Huchang Guan(关虎昌)[1], Chen Jiang(江晨)[2,†], Kailiang Xu(许凯亮)[1,3,‡], and Dean Ta(他得安)[1,3]

[1] *College of Biomedical Engineering, Fudan University, Shanghai* 200438, *China*
[2] *Yiwu Research Institute of Fudan University, Yiwu* 322000, *China*
[3] *State Key Laboratory of Integrated Chips and Systems, Fudan University, Shanghai* 201203, *China*

(Received 13 December 2025; revised manuscript received 5 February 2026; accepted manuscript online 6 February 2026)

Total focusing method (TFM) using full matrix capture (FMC) data provides high-quality ultrasound imaging by enabling pixel-level dynamic focusing during both transmission and reception. However, when applied to three-dimensional (3D) ultrasound imaging with a two-dimensional (2D) matrix array (MA), TFM suffers from computational inefficiency due to the conventional delay-and-sum (DAS) algorithm, which limits its applicability in high-volume imaging scenarios. To address this challenge, we introduce an efficient beamforming framework, designated MA-FMC-fk, leveraging the frequency-wavenumber (f-k) domain to accelerate 3D FMC imaging. The proposed method achieves a computational complexity of $O(N_u^2N_v^2N_z\log_2(N_u^2N_v^2N_z))$, compared to $O(N_u^2N_v^2N_zN_xN_y)$ for the conventional DAS algorithm. The imaging performance of the proposed method was evaluated using simulations, phantom experiments, and *in-vivo* studies. Quantitative results demonstrate that MA-FMC-fk improves the average lateral resolution by 25.00% for the simulated point targets and by 19.18% for the phantom wire experiments compared to the DAS algorithm. In addition, MA-FMC-fk enhances the average contrast-to-noise ratio (CNR) by 11.73% and the speckle signal-to-noise ratio (sSNR) by 11.16% for the phantom cyst. The MA-FMC-fk algorithm achieves a several-fold reduction in computation time on a CPU-based MATLAB platform relative to DAS. The human experimental results further demonstrate the effectiveness of the proposed method, in which the sSNR and CNR are improved by 19.74% and 18.18%, respectively. The results demonstrate that the MA-FMC-fk method improves image quality while reducing computational cost for 3D TFM imaging using a 2D matrix array.

Keywords: total focusing method, full matrix capture, frequency-wavenumber, two-dimensional matrix array

PACS: 43.80.Vj, 43.60.Tj, 87.57.nf

DOI: 10.1088/1674-1056/ae42b9 **CSTR:** 32038.14.CPB.ae42b9

1. Introduction

Three-dimensional (3D) ultrasound imaging is an advanced medical imaging modality that provides volumetric visualization of internal structures.[1,2] In general, 3D ultrasound imaging techniques are implemented through mechanical scanning,[3] freehand scanning,[4] and two-dimensional (2D) array transducers.[5,6] Mechanical scanning is achieved by mechanically controlling a one-dimensional (1D) array to move along different scanning trajectories, such as linear, tilt, and rotational scanning. Multiple cross-sectional images are sequentially acquired at varying spatial positions and then reconstructed into a 3D volumetric dataset using image processing techniques. In contrast, freehand scanning is achieved by manually moving a 1D array while tracking the probe position using position sensors. Freehand scanning offers flexible control over scanning trajectories to meet different clinical requirements. Alternatively, 2D array transducers use electronic scanning and pulse delay control to steer and focus the beam, thereby enabling the acquisition of high-frame-rate 3D ultrasound images.

Fully populated matrix arrays are a type of 2D array, featuring transducer elements arranged in a grid pattern resembling a chessboard. Each transducer element of the matrix array can be independently driven to steer and focus ultrasound beams in both lateral and elevational directions. Owing to the full sampling capability and precise beam control, matrix arrays generally offer improved image quality compared to other 2D array configurations, such as sparse arrays[7,8] and row-column addressed arrays.[9–11] Specifically, regarding the advancements in row-column addressed array (RCA) technology, Fu *et al.*[9] investigated orthogonal plane wave (OPW) compounding strategies through simulations to optimize the quality of 3D blood flow imaging. Building on these imaging methods, Sun *et al.*[10] proposed a 4D vector Doppler imaging technique utilizing ultrafast plane waves, demonstrating its capability to capture hemodynamics in the human carotid artery. Furthermore, Sun *et al.*[11] developed a single-crystal RCA transducer to achieve volumetric ultrasound localization microscopy (ULM) for super-resolved visualization of rat cerebral vasculature. 3D ultrasound using matrix arrays has been widely investigated in various studies. Gonçalves *et al.*[12] examined fetal structures, including the fetal heart, using a 2D

†Corresponding author. E-mail: Cjiang17@fudan.edu.cn
‡Corresponding author. E-mail: xukl@fudan.edu.cn

© 2026 Chinese Physical Society and IOP Publishing Ltd. All rights, including for text and data mining, AI training, and similar technologies, are reserved.

matrix array. Provost *et al.*[13] implemented 3D ultrafast ultrasound imaging using either diverging or plane waves emitted from a sparse virtual array located behind a 32×32 matrix array. Gennison *et al.*[14] performed four-dimensional (4D) shear-wave ultrasound imaging with a 32×32 matrix phased array driven by a 1024-channel ultrasound system. Rabut *et al.*[15] achieved 4D functional ultrasound imaging of the whole brain using multiple plane waves emitted from a 2D matrix array. Heiles *et al.*[16] realized volumetric ULM using a 32×32-element, 9 MHz matrix probe. Bureau *et al.*[17] performed volumetric imaging of a tissue-mimicking phantom through *ex-vivo* tissues using a 2D probe, subsequently demonstrating the potential of 3D matrix imaging for transcranial applications. Yan *et al.*[18] implemented an adaptive weight-based beamforming method to improve 3D super-resolution ultrasound imaging. Zhang *et al.*[19] investigated 3D ULM for tumor microvascular imaging using a 2D array. Wu *et al.*[20] proposed a row-transmission scheme to address the elevational blank row issue in Vermon matrix probes, improving 3D image quality and arterial wall motion estimation accuracy. Wu *et al.*[21] further introduced a projection-based directional coherence factor to reduce sidelobe artifacts by utilizing the separability of volumetric coherence given 2D aperture functions of matrix arrays. The fully populated matrix array plays an important role in ultrasound volumetric imaging.

The total focusing method (TFM)[22] is an ultrasound imaging technique that uses a full matrix capture (FMC) dataset to reconstruct high-resolution images by dynamically focusing at every point in the region of interest. However, in the case of matrix arrays, the conventional delay-and-sum (DAS) beamformer is computationally inefficient as the number of channels and pixels increases. Frequency-wavenumber (f-k) domain-based beamformers have been demonstrated to be effective methods for reducing the computational complexity of image reconstruction. The algorithm is adapted from the Fourier-domain Stolt migration algorithm, originally developed for seismic imaging[23] and subsequently applied in the fields of synthetic aperture radar (SAR) and sonar.[24,25] The method was later extended to ultrasonic imaging, facilitating further advancements in this field. In the context of 2D plane wave imaging, Lu *et al.*[26] developed a pulse-echo imaging method to achieve a high frame rate with limited diffraction beams. Garcia *et al.*[27] implemented f-k domain ultrasound imaging on plane wave echo data using an improved exploding reflector model. Bernard *et al.*[28] proposed a new ultrasound acquisition scheme based on Fourier slice imaging to achieve finer lateral resolution compared to other Fourier-based methods. Albulayli *et al.*[29] achieved plane-wave ultrasound imaging at ultrafast image acquisition rates by modifying two classical algorithms used for geophysical data processing, namely Stolt's and slant-stack depth migration under zero-offset constant velocity assumptions. Zhang *et al.*[30] extended Fourier-based techniques to the reconstruction of sectorial images from diverging wave (DW) data by proposing an explicit transformation. Regarding synthetic aperture and FMC techniques, Stepinski *et al.*[31] implemented the synthetic aperture focusing technique (SAFT) for radar and sonar in the frequency domain. Hunter *et al.*[32] introduced a Fourier-domain full matrix imaging method based on a wavenumber algorithm for ultrasonic nondestructive testing and evaluation. Vos *et al.*[33] introduced a two-stage beamforming method, combining line-based DAS with subsequent fast Fourier transform (FFT)-based beamforming, to reduce the computational load and data transfer rate for linear array systems while maintaining a comparable resolution to conventional methods. Moghimirad *et al.*[34] presented an efficient Fourier beamformer for multistatic synthetic aperture ultrasound imaging using virtual sources. Guo *et al.*[35] integrated the wavenumber beamformer with sub-Nyquist sampling, reducing the computational complexity of traditional focused ultrasound imaging. With the advancement of transducer technology, Fourier-domain algorithms have been extended from 2D to 3D imaging. Cheng *et al.*[36] adapted the high-frame-rate imaging theory for fast 3D ultrasound imaging. The results demonstrated that the processing time of Fourier beamforming using virtual sources was reduced by a factor of 20 compared to DAS. Merabet *et al.*[37] developed computationally efficient 2D and 3D reconstruction algorithms in the f-k domain to enable imaging of defects in solids. Marmonier *et al.*[38] applied Fourier-domain algorithms to 3D imaging for nondestructive testing (NDT). Lin *et al.*[39] proposed a fast Fourier-based 3D ultrasound imaging method using row and column-addressed 2D arrays, achieving reduced computational complexity. Li *et al.*[40] presented a novel Fourier-domain beamformer for 3D plane wave imaging to improve computational efficiency. Liu *et al.*[41] introduced an f-k domain beamforming strategy for efficient volumetric image reconstruction in RCA-based orthogonal plane-wave imaging. Recently, in our previous work,[42] a 3D f-k migration beamformer was proposed specifically for RCA arrays to address hardware-specific addressing constraints. However, to the best of our knowledge, the application of 3D f-k beamforming for matrix arrays, specifically in the field of medical ultrasound imaging, has received limited attention. Given the distinct requirements of medical imaging compared with NDT, such as tissue heterogeneity and resolution demands, adapting this algorithm for medical ultrasound using matrix arrays remains to be investigated.

Inspired by the challenges and limitations discussed above, this study establishes a spectral beamforming framework specifically tailored for medical ultrasound volumetric imaging with fully populated matrix arrays. Specifically,

we propose the MA-FMC-fk method to reconstruct three-dimensional full-matrix capture (3D-FMC) images, aiming to alleviate the computational burden associated with conventional DAS. By analyzing the wavefield propagation mechanism, we derive a 3D Stolt mapping theory applicable to this geometry. Consequently, this approach improves computational efficiency while enhancing spatial resolution and contrast through accurate modeling of wave diffraction, supporting the potential for real-time volumetric imaging.

The remainder of this article is structured as follows. Section 2 presents the existing work on time-domain total focusing algorithms using fully populated matrix probes. Then, the novel wavenumber beamforming algorithm is introduced. Section 3 describes the process of experimental data acquisition and the image evaluation metrics. Section 4 shows the simulation results, experimental results, and corresponding quantitative analyses. Section 5 provides further discussion. Section 6 concludes the paper.

2. Methods

FMC using matrix arrays is a specific acquisition mode for 3D ultrasound imaging, where each element sequentially transmits an ultrasonic wave while all N elements in the array simultaneously record the echoes, as shown in Fig. 1. This operation is repeated until every element has been used as the transmitter. Ultrasound imaging using FMC data provides improved image resolution and signal-to-noise ratio (SNR) compared to conventional focused and plane wave transmissions, as dynamic focusing is achieved during both transmission and reception.

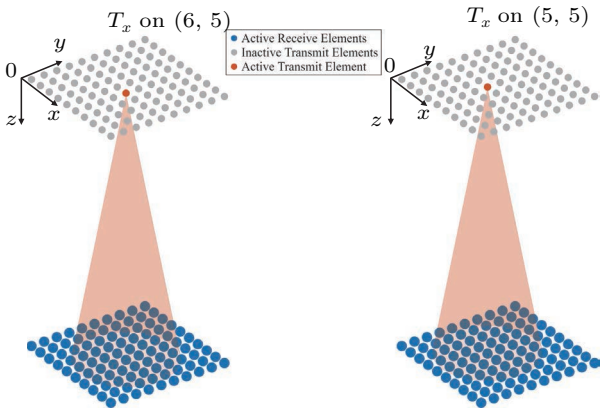


Fig. 1. FMC data acquisition model.

2.1. Delay and sum beamforming

TFM employs the DAS algorithm for beamforming, as shown in Fig. 2. For TFM using FMC data from a matrix array, the most critical step is the calculation of appropriate time delays for the DAS algorithm. To achieve focusing at each imaging voxel at (x,y,z), the algorithm must precisely compute the time-of-flight (TOF)[43] for the acoustic path from every transmitting element at $(u_x,u_y,0)$ to the voxel and back to every receiving element at $(v_x,v_y,0)$. Based on this geometric path, the TOF is expressed as

$$t_{i,j}(x,y,z) = \frac{\sqrt{(u_x-x)^2+(u_y-y)^2+z^2}}{c} + \frac{\sqrt{(v_x-x)^2+(v_y-y)^2+z^2}}{c}, \quad (1)$$

where c is the sound velocity of the propagation medium, u_x and u_y are the lateral and elevation positions of the transmitting element, respectively. v_x and v_y are the lateral and elevation positions of the receiving element, respectively. For each voxel, all delayed signals of the full matrix data are coherently summed at the imaging point to obtain the imaging point amplitude $I(x,y,z)$ as

$$I(x,y,z) = \sum_{i=1}^{N}\sum_{j=1}^{N} e_{i,j}(t_{i,j}(x,y,z)), \quad (2)$$

where $e_{i,j}(t_{i,j}(x,y,z))$ is the amplitude of the ultrasonic echo emitted by the i-th element and received by the j-th element.

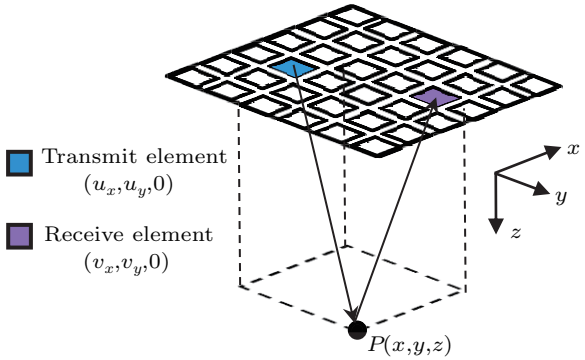


Fig. 2. Schematic of the 3D coordinate system and data acquisition geometry for the fully populated matrix array. The diagram illustrates the spatial relationship among a transmit element located at $(u_x,u_y,0)$, a receive element at $(v_x,v_y,0)$, and a spatial point $P(x,y,z)$. This geometric configuration serves as the physical basis for the conventional DAS beamformer.

2.2. Frequency-wavenumber beamforming

The f-k beamforming is a computationally efficient imaging algorithm. It first transforms the raw spatiotemporal echo data into the frequency domain via the Fourier transform. Then, leveraging the concise frequency-domain representation of the wave equation (i.e., the dispersion relation), it remaps and focuses the data to reconstruct the entire high-quality image in a single step. This approach elegantly converts the complex physical propagation process into efficient mathematical operations in the frequency domain.

According to the Weyl identity, the Green function representing the wavefield from the origin to the point (x,y,z) in a 3D Cartesian coordinate system can be expressed as

$$G(x,y,z) = \frac{\mathrm{e}^{-\mathrm{i}kr}}{r}$$

$$= \frac{1}{2\mathrm{i}\pi}\int_{-\infty}^{\infty}\int_{-\infty}^{\infty} \mathrm{e}^{-\mathrm{i}(k_x x+k_y y)}\frac{\mathrm{e}^{-\mathrm{i}k_z|z|}}{k_z}\mathrm{d}k_x\mathrm{d}k_y, \quad (3)$$

where $\mathrm{i}=\sqrt{-1}$ is the imaginary unit, $r=\sqrt{x^2+y^2+z^2}$ is the distance between the origin and the chosen point, and $k=\omega/c$ is the wavenumber. k_x, k_y, and $k_z=\sqrt{k^2-k_x^2-k_y^2}$ are the wavenumbers in the x, y, and z directions, respectively.

In 3D FMC imaging, one ultrasound pulse emitted from the transducer element located at $(u_x,u_y,0)$ is reflected by a scatterer with intensity $f(x,y,z)$ and then backscattered to be recorded by a transducer element located at $(v_x,v_y,0)$. Note that the half space $z>0$ is generally defined as the imaging area. The process can be described as

$$\begin{aligned} RF(v_x,v_y,u_x,u_y,x,y,z,\omega) &= G(x-u_x,y-u_y,z)f(x,y,z)G(x-v_x,y-v_y,z)\\ &= -\frac{1}{4\pi^2}\left(\begin{array}{l}\left(\int_{-\infty}^{\infty}\int_{-\infty}^{\infty}\mathrm{e}^{-\mathrm{i}(k_{ux}(x-u_x)+k_{uy}(y-u_y))}\frac{\mathrm{e}^{-\mathrm{i}k_{uz}z}}{k_{uz}}\mathrm{d}k_{ux}\mathrm{d}k_{uy}\right)f(x,y,z)\\ \left(\int_{-\infty}^{\infty}\int_{-\infty}^{\infty}\mathrm{e}^{-\mathrm{i}(k_{vx}(x-v_x)+k_{vy}(y-v_y))}\frac{\mathrm{e}^{-\mathrm{i}k_{vz}z}}{k_{vz}}\mathrm{d}k_{vx}\mathrm{d}k_{vy}\right)\end{array}\right), \end{aligned} \quad (4)$$

where the subscripts u and v of k refer to the wavenumbers of ultrasound transmission and backscattering, respectively. The received pulse-echo data are the responses of all scatterers in the imaging volume, expressed as a spatial integral

$$\begin{aligned} RF(v_x,v_y,u_x,u_y,\omega) &= \int_{-\infty}^{\infty}\int_{-\infty}^{\infty}\int_{-\infty}^{\infty} RF(v_x,v_y,u_x,u_y,x,y,z,\omega)\,\mathrm{d}x\,\mathrm{d}y\,\mathrm{d}z\\ &= -\frac{1}{4\pi^2}\int_{-\infty}^{\infty}\int_{-\infty}^{\infty}\int_{-\infty}^{\infty}\int_{-\infty}^{\infty}\left(\int_{-\infty}^{\infty}\int_{-\infty}^{\infty}\int_{-\infty}^{\infty}\frac{\mathrm{e}^{-\mathrm{i}(k_{ux}+k_{vx})x-\mathrm{i}(k_{uy}+k_{vy})y-\mathrm{i}(k_{uz}+k_{vz})z}}{k_{uz}k_{vz}}f(x,y,z)\,\mathrm{d}x\,\mathrm{d}y\,\mathrm{d}z\right)\mathrm{e}^{\mathrm{i}k_{ux}u_x}\\ &\quad\times\mathrm{e}^{\mathrm{i}k_{uy}u_y}\mathrm{e}^{\mathrm{i}k_{vx}v_x}\mathrm{e}^{\mathrm{i}k_{vy}v_y}\mathrm{d}k_{ux}\,\mathrm{d}k_{uy}\,\mathrm{d}k_{vx}\,\mathrm{d}k_{vy}. \end{aligned} \quad (5)$$

It is evident that the ultrasound response of the scatterers is associated with the RF data in the f-k domain, as

$$\begin{aligned} &RF(k_{ux},k_{uy},k_{vy},k_{vy},\omega)\\ &= -4\pi^2\int_{-\infty}^{\infty}\int_{-\infty}^{\infty}\int_{-\infty}^{\infty}\frac{\mathrm{e}^{-\mathrm{i}k_X x-\mathrm{i}k_Y y-\mathrm{i}k_Z z}}{k_{uz}k_{vz}}f(x,y,z)\,\mathrm{d}x\mathrm{d}y\mathrm{d}z, \end{aligned} \quad (6)$$

where $k_X=k_{ux}+k_{vx}$, $k_Y=k_{uy}+k_{vy}$, and $k_Z=\sqrt{k^2-k_{ux}^2-k_{uy}^2}+\sqrt{k^2-k_{vx}^2-k_{vy}^2}$ are the wavenumber baselines in the three directions of the scatterers.

The propagating wavenumber can be calculated using the wavenumber baseline, which is related to the distribution of the scatterers as

$$k=\frac{\sqrt{(k_Z^2+k_{ux}^2+k_{uy}^2+k_{vx}^2+k_{vy}^2)^2-4(k_{ux}^2+k_{uy}^2)(k_{vx}^2+k_{vy}^2)}}{2k_z}. \quad (7)$$

Using interpolation methods, the intensity of scatterers in the wavenumber domain can be recovered from the radio-frequency (RF) data. The ultrasound image is obtained using a 3D inverse Fourier transform.

The flowchart of 3D ultrasound imaging using the MA-FMC-fk method is given in detail in Fig. 3. The following steps outline the proposed algorithm.

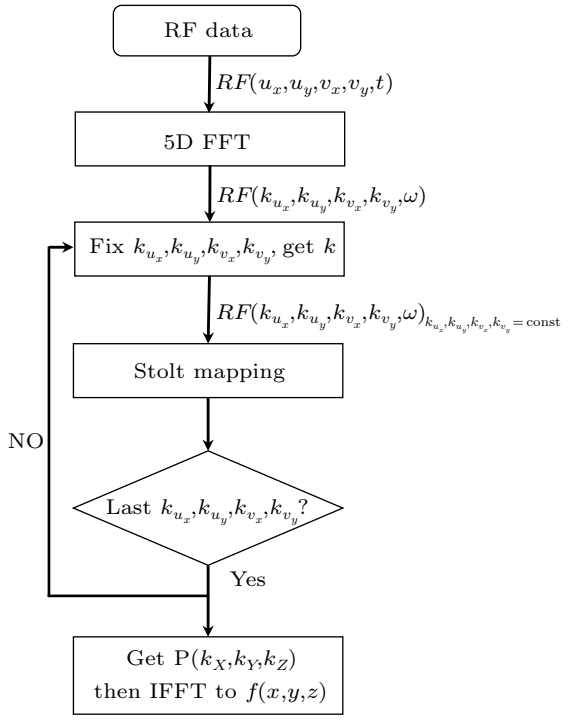


Fig. 3. Flowchart of the MA-FMC-fk method.

(i) The time-space data $RF(u_x,u_y,v_x,v_y,t)$ are converted to wavenumber-frequency data $RF(k_{ux},k_{uy},k_{vx},k_{vy},\omega)$ using a

five-dimensional FFT.

(ii) The wavenumber k is calculated at each wavenumber sampling point $(k_{ux}, k_{uy}, k_{vx}, k_{vy})$ using Eq. (7). A 1D slice of $RF(k_{ux}, k_{uy}, k_{vx}, k_{vy}, \omega)$ is obtained in the wavenumber-frequency domain.

(iii) The 1D slices are interpolated to the image wavenumber domain $P(k_{ux}, k_{uy}, k_{vx}, k_{vy}, k_z)$ using Stolt mapping.

(iv) The interpolated 1D slices are summed to produce the wavenumber-domain data $P(k_X, k_Y, k_Z)$ of the 3D image.

(v) The 3D data in the wavenumber domain are converted into a 3D ultrasound image by a 3D inverse Fourier transform in the spatial domain.

3. Experiment setup

3.1. Data acquisition

The performance of the proposed method was validated through simulations, tissue-mimicking phantom experiments, and *in vivo* studies. The RF data were acquired using the simulation mode of a Vantage NXT 4 system (Verasonics Inc., Kirkland, WA, USA), equipped with a 32×32 matrix array probe with uniform element spacing. Five ideal point targets, modeled as mathematical points with infinitesimal size, were used to assess the resolution of the point spread function (PSF) in the simulations. The targets were located at (0 mm, 0 mm) in the lateral and elevational directions and uniformly distributed from 10 mm to 30 mm along the axial direction. The simulation parameters were configured with a sound speed of 1540 m/s and an attenuation coefficient of $0.5\ \mathrm{dB \cdot cm^{-1} \cdot MHz^{-1}}$ for the propagation medium.

To evaluate the imaging performance, experiments were conducted using a multi-purpose ultrasound phantom (Model 040GSE, CIRS Inc., Norfolk, VA, USA). The phantom is constructed from a proprietary solid elastic hydrogel, calibrated to a sound speed of 1540 m/s and an attenuation coefficient of $0.5\ \mathrm{dB \cdot cm^{-1} \cdot MHz^{-1}}$. While the phantom contains multiple target groups, specific targets were selected in this study to validate the proposed method. For spatial resolution assessment, the vertical distance group was imaged. This group consists of nylon monofilaments with a diameter of 0.1 mm. Specifically, the wire targets located within the depth range of 10 mm to 30 mm, with a 10 mm spacing, were selected for analysis. For contrast assessment, an anechoic stepped cylinder target located at a depth of 15 mm was selected to simulate a fluid-filled lesion. A coupling agent was applied to eliminate air gaps between the transducer surface and the phantom. For data acquisition, the Vantage NXT 4 system was connected to the 32×32 matrix probe. However, to meet the uniform element spacing requirement ($\lambda/2$ pitch) inherent to the Fourier transform-based f-k algorithm, the system was configured to activate only an 8×32 rectangular sub-aperture of the matrix array for signal transmission and reception. Further validation was performed by scanning the carotid artery of a healthy volunteer. Informed consent was obtained prior to the experiment. The data were acquired using a hand-held probe under normal breathing conditions. The *in vivo* data were acquired using the same experimental configuration as the phantom study, utilizing the active 8×32 rectangular sub-aperture of the matrix probe driven by the Vantage NXT 4 system. Acquisition parameters for all experiments are summarized in Table 1.

Table 1. Parameters of the transducer for simulation and experiment.

	Simulation	Experiment
Element number	32×32	8×32
Center frequency	3.47 MHz	3.47 MHz
Fractional bandwidth	60%	60%
Pitch	0.3 mm	0.3 mm
Element length	0.275 mm	0.275 mm
Sampling frequency	13.90 MHz	13.90 MHz

3.2. Image quality evaluation metrics

A suite of image quality metrics was employed to quantitatively evaluate the two imaging algorithms. Full-width at half-maximum (FWHM) was used to quantify resolution by measuring the -6 dB width of the point-target amplitude profile curve. Contrast ratio (CR) was used to quantify the contrast between different tissues, defined as the ratio of the average pixel intensity of the cyst to that of the background speckle. The contrast-to-noise ratio (CNR) assesses the detectability of the target by calculating the ratio of the pixel intensity difference between the cyst and the background noise to the square root of the sum of the standard deviations of the pixel intensities. The speckle signal-to-noise ratio (sSNR) was used to evaluate speckle uniformity, defined as the ratio of the mean to the standard deviation of the pixel intensity within the speckle region. To avoid changes in dynamic range affecting the assessment of image quality, the generalized contrast-to-noise ratio (gCNR) was introduced to improve lesion detectability.[44] Unlike traditional CNR, gCNR is no longer affected by logarithmic compression, as it compares the pixel intensity distributions in two different regions. The mathematical definitions for these metrics are as follows:

$$\mathrm{CR} = 20\log_{10}\left(\frac{u_\mathrm{i}}{u_\mathrm{b}}\right), \tag{8}$$

$$\mathrm{CNR} = \frac{|u_\mathrm{i} - u_\mathrm{b}|}{\sqrt{\sigma_\mathrm{i}^2 + \sigma_\mathrm{b}^2}}, \tag{9}$$

$$\mathrm{sSNR} = \frac{u_\mathrm{b}}{\sigma_\mathrm{b}}, \tag{10}$$

$$\mathrm{gCNR} = 1 - \int \min\{p_\mathrm{i}(x), p_\mathrm{b}(x)\}\,\mathrm{d}x, \tag{11}$$

where u_i and u_b denote the mean pixel intensities of the cyst region and the background speckle area, respectively. σ_i and

σ_b represent their corresponding standard deviations. p_i and p_b refer to the probability distributions of the cyst region and the speckle area, respectively.

4. Results

4.1. Point simulation

Both methods accurately reconstruct the positions of the simulated point scatterers, as illustrated in the 3D images in Figs. 4(a) and 4(f). The tri-plane views are further shown from different angles in Figs. 4(e) and 4(j). The results indicate that the main lobe width of the point targets in the images reconstructed by the DAS method broadens as depth increases. In contrast, the main lobe width obtained using the MA-FMC-fk remains relatively stable across different depths, as shown in Fig. 4(f). Notably, in the shallow region, the MA-FMC-fk displays an elevated sidelobe level. Conversely, in the deep region, the DAS-reconstructed images exhibit higher sidelobe levels compared to those of the MA-FMC-fk. Figures 4(b)–4(d) and 4(g)–4(i) further visualize the 2D cross-sectional slices of the point targets along three orthogonal planes. As shown in Figs. 4(b) and 4(g), the main lobe width of the DAS image is larger than that of the MA-FMC-fk method, indicating that the latter offers superior lateral resolution.

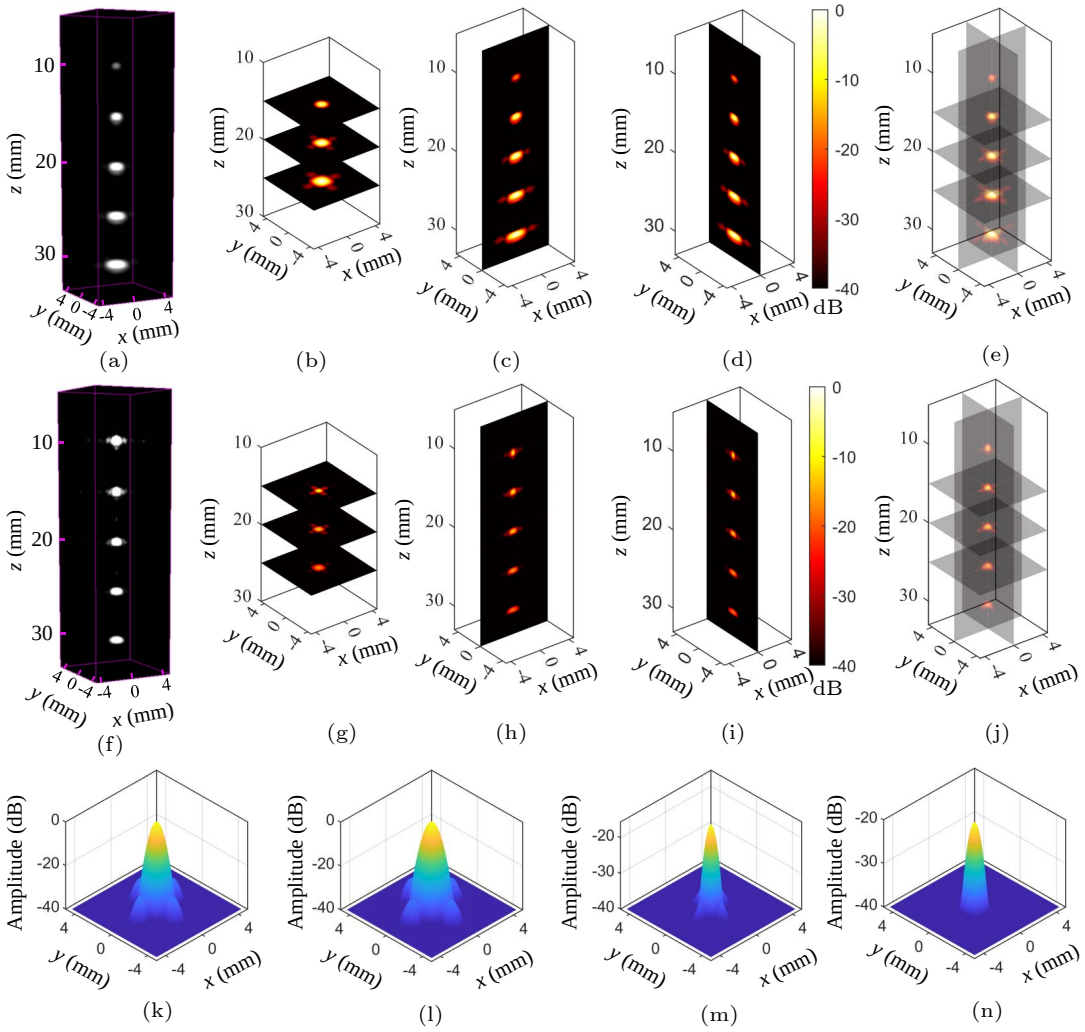


Fig. 4. Imaging results of simulated point targets obtained using the conventional DAS (a)–(e) and the proposed MA-FMC-fk (f)–(j) methods. (a) and (f) 3D volumetric renderings; (b) and (g) lateral-elevation (xy-plane) slices at depths of 15 mm, 20 mm, and 25 mm; (c) and (h) lateral-axial (xz-plane) slices at $y = 0$ mm; (d) and (i) elevation-axial (yz-plane) slices at $x = 0$ mm; and (e) and (j) tri-plane views. (k) and (l) 3D beam profiles of the DAS method at depths of 25 mm and 30 mm, respectively, and (m) and (n) corresponding profiles of the MA-FMC-fk method.

Table 2. Quantification of the lateral FWHM is performed using both simulated point targets and experimental wire phantom data in lateral-axial slices at $y = 0$ mm.

	Simulated point targets					Experimental wire phantom		
Location[mm]	(0, 10)	(0, 15)	(0, 20)	(0, 25)	(0, 30)	(0, 10)	(0, 19.2)	(0, 28.6)
DAS[mm]	0.74	0.74	0.89	1.12	1.32	0.41	0.71	1.06
MA-FMC-fk[mm]	0.36	0.55	0.71	0.91	1.09	0.33	0.59	0.85

The 3D beam profiles for the DAS method at depths $z = 25$ mm and $z = 30$ mm are given in Figs. 4(k) and 4(l), respectively, with the corresponding results for MA-FMC-fk presented in Figs. 4(m) and 4(n). It can be seen that the MA-FMC-fk method achieves a narrower main lobe width and a lower sidelobe level, indicating advantages in both lateral resolution enhancement and sidelobe suppression performance. The proposed MA-FMC-fk method demonstrates superior spatial resolution, as quantified by FWHM in Table 2. Specifically, it achieves an average FWHM of 0.72 mm, representing a 25.00% improvement over the 0.96 mm obtained using the DAS method.

4.2. Wire phantom experiments

The 3D ultrasound images of the wire phantom reconstructed using different methods are shown in Figs. 5(a) and 5(f). Although the embedded wires are rendered consistently by both approaches, the images generated by the MA-FMC-fk method exhibit a reduction in signal intensity in the deeper region compared with the DAS reconstruction. Furthermore, the experimental wire phantom targets are clearly visualized in the tri-planar views presented in Figs. 5(e) and 5(j).

The three corresponding orthogonal 2D slices of the wire phantom for the DAS and MA-FMC-fk methods are depicted in Figs. 5(b)–5(d) and 5(g)–5(i), respectively. A visual inspection of the lateral-axial (x-z) plane (Figs. 5(c) and 5(h)) reveals that the MA-FMC-fk method produces a narrower main lobe, indicating enhanced spatial resolution over the conventional DAS method. To quantify this improvement, a comparative analysis of the lateral amplitude profiles was performed at depths of $z = 19.2$ mm and 28.6 mm, as shown in Figs. 5(k)–5(n). The lateral FWHM for each method is listed in Table 2, showing that the MA-FMC-fk method consistently yields lower lateral FWHM values. The average FWHM for all wire targets was measured to be 0.73 mm for DAS and 0.59 mm for MA-FMC-fk, representing an improvement of 19.18%.

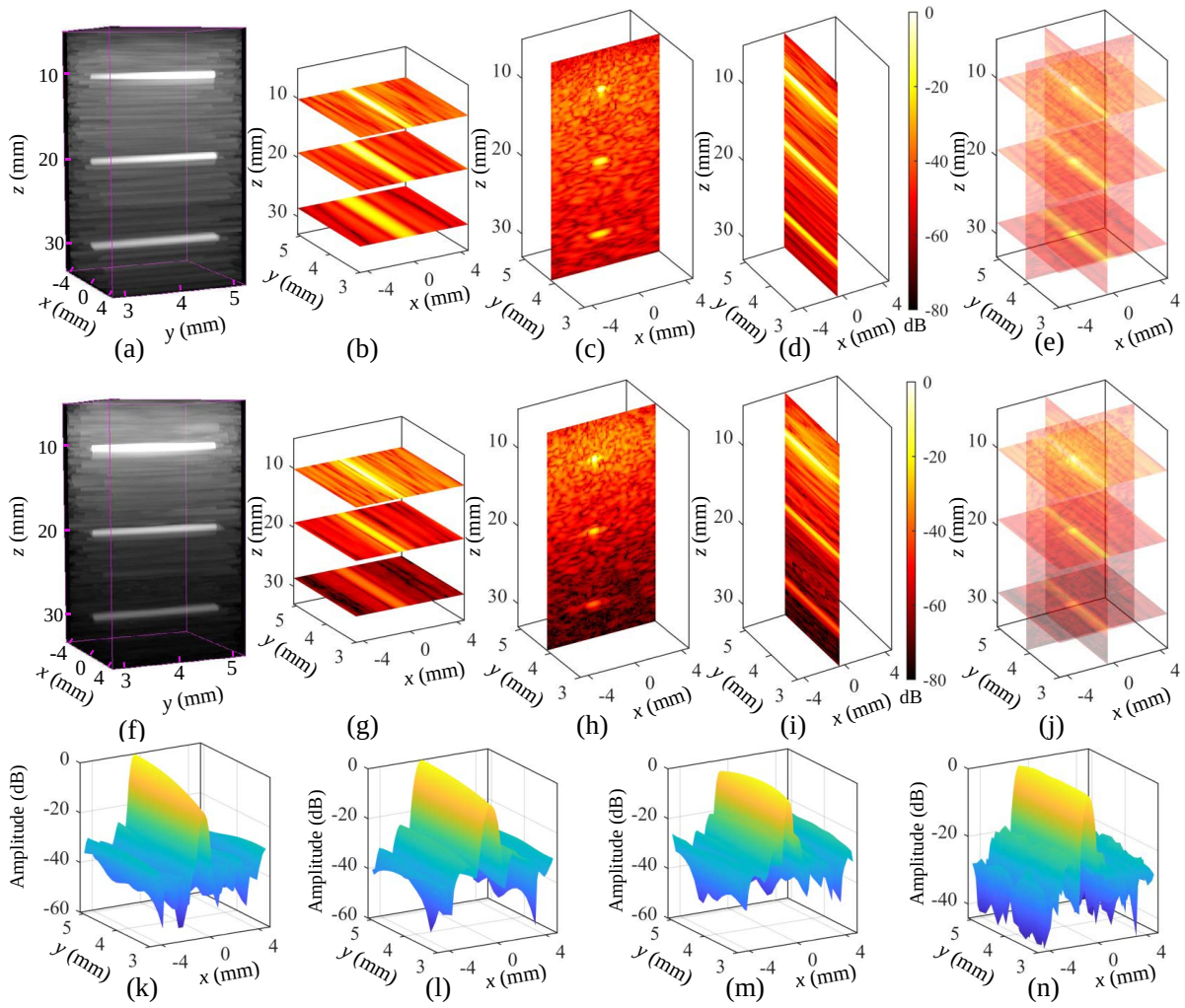


Fig. 5. Imaging results of the experimental wire phantom obtained using the conventional DAS (a)–(e) and the proposed MA-FMC-fk (f)–(j) methods. (a) and (f) 3D volumetric renderings; (b) and (g) lateral-elevation (xy-plane) slices at depths of 10.1 mm, 19.2 mm, and 28.6 mm; (c) and (h) lateral-axial (xz-plane) slices at $y = 4.12$ mm; (d) and (i) elevation-axial (yz-plane) slices at $x = -0.51$ mm; and (e) and (j) tri-plane views. (k) and (l) 3D beam profiles of the DAS method at depths of 19.2 mm and 28.6 mm, respectively, and (m) and (n) corresponding profiles of the MA-FMC-fk method.

4.3. Cyst phantom experiments

The 3D ultrasound images of the experimental phantom with cyst targets reconstructed using different methods are presented in Figs. 6(a) and 6(c). The tri-plane views (Figs. 6(b) and 6(d)) and corresponding 2D orthogonal slices (Figs. 6(e)–6(g) for DAS and Figs. 6(i)–6(k) for MA-FMC-fk) are also provided, revealing the details of the cyst morphological features from various observation angles. The image reconstructed by the DAS algorithm suffers from noise artifacts within the anechoic cyst (Fig. 6(f)). In contrast, the MA-FMC-fk method improves the imaging quality. The reconstructed image not only suppresses the internal noise of the cyst (Fig. 6(j)), but also enhances edge sharpness, contributing to accurate detection of the target. To further evaluate the contrast performance, the 3D beam profiles at a depth of 14.9 mm are also presented in Figs. 6(h) and 6(l) for the DAS and MA-FMC-fk methods, respectively.

The imaging performance of the different methods was systematically evaluated using four quantitative metrics (CR, CNR, sSNR, and gCNR), as listed in Table 3. The cyst and speckle regions for calculating these metrics are indicated by a black circle and a blue rectangle, respectively, as shown in Fig. 6(f). The MA-FMC-fk method outperforms the DAS algorithm, improving CNR by 11.73% and sSNR by 11.16%. The CR and gCNR achieved by both methods are nearly identical. These results indicate that the MA-FMC-fk method can effectively maintain the speckle texture features while enhancing cyst contrast.

Table 3. CR, CNR, sSNR, and gCNR for experimental cyst phantom and human carotid artery.

	Experimental cyst phantom				Human carotid artery			
	CR	CNR	sSNR	gCNR	CR	CNR	sSNR	gCNR
DAS	21.59	1.96	2.15	0.9666	16.71	0.66	0.76	0.5607
MA-FMC-fk	20.02	2.19	2.23	0.9674	17.13	0.78	0.91	0.5662

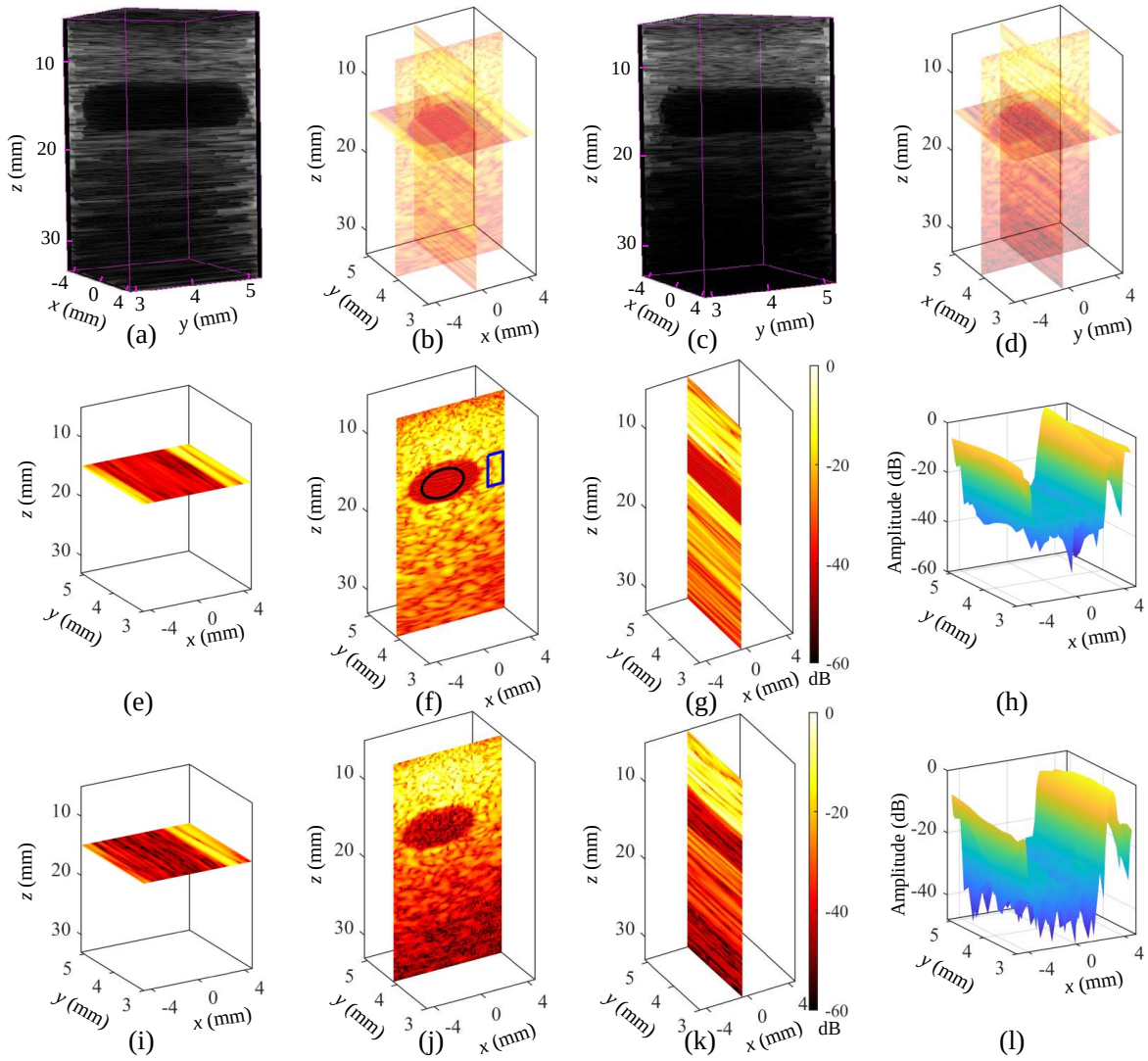


Fig. 6. Imaging results of the cyst phantom obtained using the conventional DAS (a), (b), (e)–(g) and the proposed MA-FMC-fk (c), (d), (i)–(k) methods. (a) and (c) 3D volumetric renderings; (b) and (d) tri-plane views; (e) and (i) lateral-elevation (xy-plane) 2D slices at a depth of $z = 14.9$ mm; (f) and (j) axial-lateral (xz-plane) 2D slices at $y = 4.1$ mm; and (g) and (k) elevation-axial (yz-plane) 2D slices at $x = -0.51$ mm. (h) and (l) 3D beam profiles at a depth of 14.9 mm for the DAS and MA-FMC-fk methods, respectively.

4.4. *In vivo* study

As shown in Fig. 7, the experimental platform utilized a Vantage NXT 4 system configuration for the *in vivo* imaging scenario. Figure 8 presents the ultrasound imaging results of the carotid artery obtained using different reconstruction methods. The volumetric renderings and tri-plane views are shown in Figs. 8(a)–8(d), while the associated 2D slices for the DAS and MA-FMC-fk methods are displayed in Figs. 8(e)–8(g) and 8(i)–8(k), respectively. The corresponding 3D beam profiles at a depth of 13.6 mm are shown in Figs. 8(h) and 8(l). The longitudinal and transverse views clearly display the arterial anatomy in 2D slices. Both methods exhibit limited performance in suppressing noise; therefore, noise and clutter remain observable within the vessel lumen. In contrast, the MA-FMC-fk image displays a smoother speckle pattern and reveals well-defined hyperechoic tissues.

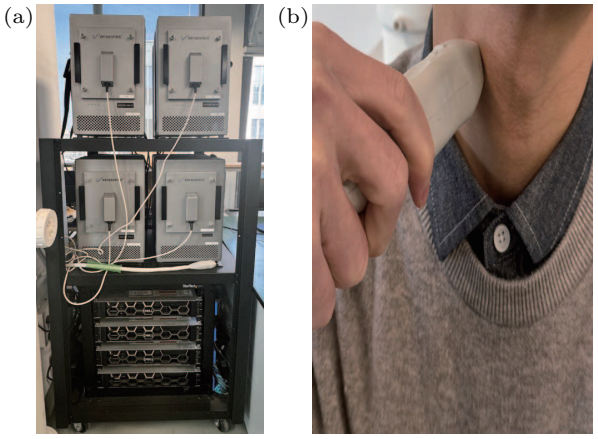


Fig. 7. Experimental data acquisition platform and *in vivo* imaging scenario. (a) The Vantage NXT 4-system configuration equipped with 1024 transmit and receive channels. (b) *In vivo* scanning of a healthy young male volunteer using a fully addressed 2D matrix array with a center frequency of 3 MHz.

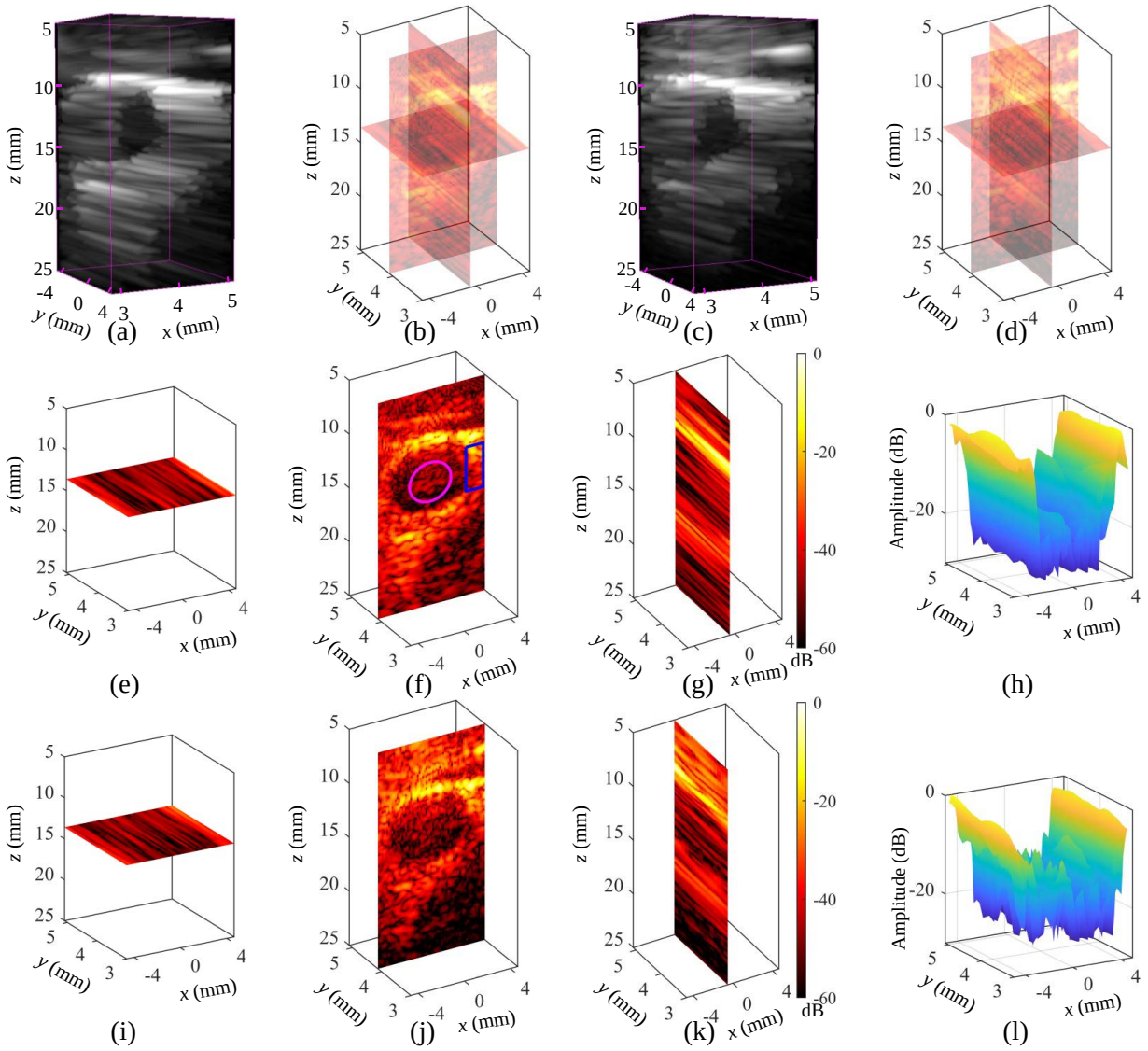


Fig. 8. Imaging results of the carotid artery reconstructed using the conventional DAS (a), (b), (e)–(g) and the proposed MA-FMC-fk (c), (d), (i)–(k) methods. (a) and (c) 3D volumetric renderings; (b) and (d) tri-plane views; (e) and (i) lateral-elevation (xy-plane) 2D slices at a depth of $z = 13.6$ mm; (f) and (j) axial-lateral (xz-plane) 2D slices at $y = 4.1$ mm; and (g) and (k) elevation-axial (yz-plane) 2D slices at $x = -0.51$ mm. (h) and (l) 3D beam profiles at a depth of 13.6 mm for the DAS and MA-FMC-fk methods, respectively.

For the quantitative evaluation, as shown in Fig. 8(f), the vessel region and the tissue region are delineated by a magenta circle and a blue rectangle, respectively, for measuring the CR, CNR, sSNR, and gCNR metrics. The results are shown in Table 3. The experimental results indicate that the MA-FMC-fk method improves CNR by 18.18% and sSNR by 19.74% compared to the DAS method, while the CR and gCNR for the two methods are almost the same. These findings suggest that the MA-FMC-fk method enhances target detectability while maintaining tissue homogeneity.

4.5. Computational complexity analysis

The remarkable advantage of the MA-FMC-fk method is its operation entirely in the Fourier domain, which allows for improved computational efficiency over the DAS approach. The theoretical computational performance of the two methods is quantitatively analyzed. The computational complexity is characterized using the Landau symbol O. Here, N_u and N_v are defined as the numbers of elements in the lateral and elevational directions of the 2D array transducer, respectively. K represents the number of time samples acquired by the array elements. Furthermore, N_x, N_y, and N_z denote the numbers of voxels in the lateral, elevational, and axial dimensions of the 3D image, respectively. For FMC, a five-dimensional dataset of size $N_u \times N_u \times N_v \times N_v \times K$ is obtained. For the MA-FMC-fk method, spatial-temporal data acquired by the matrix array are first zero-padded and then transformed into the f-k domain via a five-dimensional (5D) FFT, with a computational complexity of $O(N_u^2 N_v^2 K \log_2(N_u^2 N_v^2 K))$. Subsequently, a one-dimensional slice of the Fourier-transformed data is obtained at each wavenumber sampling point $(k_{ux}, k_{uy}, k_{vx}, k_{vy})$, and then interpolated and summed. Finally, the data in the wavenumber domain are transformed to the spatial domain by a 3D inverse Fourier transform. The computational costs for interpolation, summation, and 3D inverse Fourier transform are denoted as $O(N_u N_v N_z N_x N_y)$, $O(N_u N_v N_z N_x N_y)$, and $O(N_z N_x N_y \log_2(N_z N_x N_y))$, respectively. N_u is generally equivalent to N_x, and N_v to N_y, while K is typically a multiple of N_z. Furthermore, the cost of the 3D inverse Fourier transform is negligible compared with that of the 5D Fourier transform. Therefore, the computational complexity of MA-FMC-fk is $O(N_u^2 N_v^2 N_z \log_2(N_u^2 N_v^2 N_z))$. In contrast, the DAS method executes 1D linear interpolation along the temporal axis of RF data for each voxel and every transmit-receive pair, leading to a computational complexity of $O(N_u^2 N_v^2 N_z N_x N_y)$. Theoretical analysis thus confirms that the MA-FMC-fk method achieves lower computational costs compared to DAS, which is particularly advantageous for large-scale ultrasound imaging applications requiring high-dimensional data processing. This translates to a computational speed improvement by a factor of approximately N_u over DAS, often resulting in a performance increase of several orders of magnitude. From a theoretical perspective, the wavenumber-domain MA-FMC-fk algorithm is derived by constructing the forward propagation model of the wave equation and solving its inverse problem. Its mathematical rigor is superior to that of the empirically based DAS beamforming. Numerical simulations show that the PSF obtained by the proposed method exhibits superior spatial resolution and characterization. This performance is further confirmed by experimental measurements using FMC data from a 3.47 MHz 2D transducer, where the results agree well with theoretical predictions.

The computational performance of the two algorithms was evaluated by reconstructing 3D images offline in MATLAB on a workstation equipped with an Intel Xeon Silver 4110 CPU (2.10 GHz) and 1 TB of RAM. To minimize computational cost, the code was vectorized, and MATLAB's built-in *interp1* and *fftn* functions were employed. The computation time for each method as a function of the total number of image voxels is shown in Table 4. For the simulation analysis, the number of voxels in the lateral and elevational directions was set to 64, while the number of axial voxels ranges from 16 to 256. Similarly, in the phantom and *in vivo* studies, the lateral and elevational voxel counts are 64 and 16, respectively, while the axial voxel counts vary from 64 to 1024. The experimental results demonstrate that the MA-FMC-fk approach exhibits a computational efficiency advantage over conventional DAS beamforming. Notably, the temporal discrepancy between the two algorithms widens nonlinearly as the number of voxels increases. Specifically, the MA-FMC-fk beamformer achieves a 2.1-fold speedup at 2^{16} voxels, which extends to 11.6-fold at 2^{20} voxels. This phenomenon stems from the fundamental algorithmic differences between the two algorithms. At lower voxel counts, the computational cost is dominated by 5D FFT operations and phase calibration procedures. The observed growth in computation time is highly consistent with theoretical predictions of computational complexity. However, it must be emphasized that practical computation times are also substantially influenced by critical parameters such as hardware capabilities, code optimization, and data throughput, which can account for performance variations across different implementations.

Table 4. Summary of the computational performance of the MA-FMC-fk and DAS algorithms under different voxel resolutions. The theoretical computational complexity of the MA-FMC-fk algorithm is $O(N_u^2 N_v^2 N_z \log_2 N_u^2 N_v^2 N_z)$, whereas that of the DAS algorithm is $O(N_u^2 N_v^2 N_x N_y N_z)$.

Voxel counts	MA-FMC-fk runtime (s)	DAS runtime (s)	Acceleration ratio
2^{16}	1409	2952	2.1×
2^{17}	2291	6363	2.8×
2^{18}	2948	12287	4.2×
2^{19}	3442	22777	6.6×
2^{20}	4538	52594	11.6×

5. Discussion

This study addressed the high computational cost associated with TFM-based 3D ultrasound imaging, which is severely limited by the conventional DAS algorithm despite its excellent image quality resulting from dynamic focusing. The primary contribution of this work was the implementation and validation of a computationally efficient f-k migration beamformer for 3D FMC data acquired with a 2D matrix array. The efficacy and performance of the proposed method were rigorously evaluated against the benchmark DAS-based TFM through a comprehensive methodology involving numerical simulations, wire phantom experiments, and *in vivo* studies.

The MA-FMC-fk demonstrates superior performance compared to conventional DAS in terms of both contrast and resolution. This is consistently observed in imaging results from point-target simulations and wire phantom experiments, where the DAS method yields lower resolution. This performance discrepancy can be attributed to fundamental differences in the theoretical frameworks of the two methods, despite their shared use of a spherical wavefront propagation model[45] and double dynamic focusing to optimize image quality. DAS is a diffraction-based field reconstruction algorithm rooted in the principle of wave superposition. While advantageous for its simplicity and universality, the method is primarily limited by insufficient compensation for wavefront energy attenuation during signal synthesis, leading to inaccurate characterization of scatterer features. In contrast, the MA-FMC-fk method constructs a complete inverse scattering mathematical model based on the spatial mapping theory of the Green function solution of the wave equation. This wavefield inverse propagation algorithm not only corrects phase deviations but also introduces an accurate amplitude compensation mechanism, thereby accounting for the enhanced spatial resolution and contrast achieved by the MA-FMC-fk method.

As observed in the imaging results from the wire-target phantom, cyst phantom, and carotid artery experiments, the MA-FMC-fk method exhibits lower intensity in deeper regions compared to the DAS method. This discrepancy is a direct consequence of their fundamentally different image formation strategies. The strategy for DAS can be described as an accumulative enhancement model, reconstructing each pixel by summing the RF data from all relevant transmit-receive pairs. This inherent accumulation effect results in a systematic growth of image intensity as the imaging depth increases owing to the greater number of signals participating in the summation. In contrast, the MA-FMC-fk method employs a global mapping model requiring no summation. Instead, it transforms the entire dataset into the f-k domain, establishing a precise mapping between the data and image voxels based on the wave equation, thereby redistributing energy to the correct spatial locations. Consequently, this method does not inherently produce depth-dependent intensity gain, and its final intensity distribution relies on external time gain compensation (TGC) for adjustment.

It should be emphasized that the comparative performance evaluation among algorithms is dependent on specific implementation platforms. This study demonstrates that the MA-FMC-fk beamformer consistently outperforms the DAS beamformer in terms of computational efficiency. Since both algorithms were implemented on the MATLAB platform, which excels at efficient block processing but is less efficient with loop operations, the MA-FMC-fk algorithm gained a distinct advantage. If implemented in a language such as C, the advantage of the f-k domain algorithm might be diminished. Nevertheless, both theoretical analysis and experimental results confirm that the MA-FMC-fk algorithm holds a clear efficiency advantage over the time-domain DAS algorithm when processing large-scale datasets.

It should be noted that FMC imaging using matrix arrays is subject to a reduced frame rate, as the number of transmission events equals the number of transmit elements. Regarding computational implementation, the proposed method incurs higher memory overhead than conventional DAS, as it requires storing both the RF dataset and the 5D spectral data in device memory. However, as illustrated in the MA-FMC-fk flowchart, the algorithm relies on four independent nested loops, making the structure suitable for parallelization on graphics processing units (GPUs). Detailed code-level optimization and validation of this parallel efficiency will be the subject of future work.

Unlike the straightforward implementation of time-domain DAS, the wavenumber-domain MA-FMC-fk involves a more intricate processing pipeline. Consequently, rigorous parameter optimization, particularly for wavenumber interpolation, is essential to preserve image quality in deeper regions. Conversely, despite its computational cost, DAS benefits from conceptual simplicity and ease of implementation, making it adaptable to complex geometries such as curved arrays. Extending Fourier-domain algorithms to such non-planar configurations remains a challenge for future investigation.

6. Conclusion

This study presents a 3D ultrasound imaging framework utilizing FMC data acquired via a 2D matrix array. To address the heavy computational cost of traditional DAS beamforming, we propose an MA-FMC-fk beamformer that leverages efficient f-k domain processing. Comprehensive validation through simulations, phantom studies, and *in vivo* experiments indicates that this technique not only significantly accelerates image reconstruction but also yields superior image quality,

characterized by enhanced resolution, contrast, and more homogeneous speckle patterns. These results suggest that adapting f-k beamforming for matrix arrays in medical ultrasound offers a robust pathway toward high-quality, real-time volumetric ultrasound imaging.

Acknowledgments

Project supported by the National Natural Science Foundation of China (Grant No. 12574495), the National Key Research and Development Program of China (Grant No. 2023YFC2410900), and the Natural Science Foundation of Gansu Province (Grant No. 25JRRG038).

References

[1] Huang Q and Zeng Z 2017 *BioMed Res. Int.* **2017** 6027029
[2] Fenster A and Downey D B 2002 *IEEE Eng. Med. Biol. Mag.* **15** 41
[3] Chang C C, Chen P Y, Huang H and Huang C C 2018 *IEEE Trans. Biomed. Eng.* **66** 1742
[4] Chung S W, Shih C C and Huang C C 2017 *Ultrasonics* **74** 11
[5] Fenster A and Downey D B 2000 *Annu. Rev. Biomed. Eng.* **2** 457
[6] Correia M, Provost J, Tanter M and Pernot M 2016 *Phys. Med. Biol.* **61** L48
[7] Ramalli A, Boni E, Roux E, Liebgott H and Tortoli P 2022 *IEEE Trans. Ultrason. Ferroelectr. Freq. Control* **69** 2739
[8] Masoumi M H, Kaddoura T and Zemp R J 2023 *IEEE Trans. Ultrason. Ferroelectr. Freq. Control* **70** 460
[9] Fu Y P, Sun Q D, Li B Y, Ta D A and Xu K L 2023 *Acta Phys. Sin.* **72** 074302 (in Chinese)
[10] Sun Q, Fu Y, Yan S and Xu K 2025 *IEEE Trans. Ultrason. Ferroelectr. Freq. Control* **72** 202
[11] Sun Q, Hou S, He R, Fu Y, Wu J, Dai J and Xu K 2025 *IEEE Trans. Ultrason. Ferroelectr. Freq. Control* **72** 698
[12] Gonçalves L F, Espinoza J, Kusanovic J P, Lee W, Nien J K, Santolaya-Forgas J, Mari G, Treadwell M C and Romero R 2006 *J. Ultrasound Med.* **25** 745
[13] Provost J, Papadacci C, Arango J E, Imbault M, Fink M, Gennisson J L, Tanter M and Pernot M 2014 *Phys. Med. Biol.* **59** L1
[14] Gennisson J L, Provost J, Deffieux T, Papadacci C, Imbault M, Pernot M and Tanter M 2015 *IEEE Trans. Ultrason. Ferroelectr. Freq. Control* **62** 1059
[15] Rabut C, Correia M, Finel V, Pezet S, Pernot M, Deffieux T and Tanter M 2019 *Nat. Methods* **16** 994
[16] Heiles B, Correia M, Hingot V, Pernot M, Provost J, Tanter M and Couture O 2019 *IEEE Trans. Med. Imaging* **38** 2005
[17] Bureau F, Robin J, Le Ber A, Lambert W, Fink M and Aubry A 2023 *Nat. Commun.* **14** 6793
[18] Yan J, Wang B, Riemer K, Hansen-Shearer J, Lerendegui M, Toulemonde M, Rowlands C J, Weinberg P D and Tang M X 2023 *IEEE Trans. Biomed. Eng.* **70** 2752
[19] Zhang C, Lei S, Ma A, Wang B, Wang S, Liu J, Shang D, Zhang Q, Li Y, Zheng H and Ma T 2024 *Eur. Radiol.* **34** 5250
[20] Wu X and Lee W N 2024 *IEEE Trans. Ultrason. Ferroelectr. Freq. Control* **71** 659
[21] Wu X and Lee W N 2025 *IEEE Trans. Ultrason. Ferroelectr. Freq. Control* **72** 817
[22] Sun L J, Han Q B and Jin Q L 2025 *Chin. Phys. B* **34** 014301
[23] Stolt R H 1978 *Geophysics* **43** 23
[24] Cafforio C, Prati C and Rocca F 2002 *IEEE Trans. Aerosp. Electron. Syst.* **27** 194
[25] Soumekh M 2002 *IEEE Signal Process. Mag.* **12** 21
[26] Lu J Y 1997 *IEEE Trans. Ultrason. Ferroelectr. Freq. Control* **44** 839
[27] Garcia D, Le Tarnec L, Muth S, Montagnon E, Porée J and Cloutier G 2013 *IEEE Trans. Ultrason. Ferroelectr. Freq. Control* **60** 1853
[28] Bernard O, Zhang M, Varray F, Gueth P, Thiran J P, Liebgott H and Friboulet D 2014 *Proc. IEEE Int. Ultrason. Symp. (Chicago)* p. 129
[29] Albulayli M and Rakhmatov D 2018 *IEEE Trans. Ultrason. Ferroelectr. Freq. Control* **65** 1321
[30] Zhang M, Varray F, Besson A, Carrillo R E, Viallon M, Garcia D, Thiran J P, Friboulet D, Liebgott H and Bernard O 2016 *IEEE Trans. Ultrason. Ferroelectr. Freq. Control* **63** 2125
[31] Stepinski T 2007 *IEEE Trans. Ultrason. Ferroelectr. Freq. Control* **54** 1399
[32] Hunter A J, Drinkwater B W and Wilcox P D 2008 *IEEE Trans. Ultrason. Ferroelectr. Freq. Control* **55** 2450
[33] Vos H J, van Neer P L, Mota M M, Verweij M D, van der Steen A F and Volker A W 2015 *IEEE Trans. Ultrason. Ferroelectr. Freq. Control* **63** 60
[34] Moghimirad E, Hoyos C A V, Mahloojifar A, Asl B M and Jensen J A 2016 *IEEE Trans. Ultrason. Ferroelectr. Freq. Control* **63** 2018
[35] Guo H, Freear S and Zhou G Q 2024 *IEEE Trans. Ultrason. Ferroelectr. Freq. Control* **71** 972
[36] Cheng J and Lu J Y 2006 *IEEE Trans. Ultrason. Ferroelectr. Freq. Control* **53** 880
[37] Merabet L, Robert S and Prada C 2019 *IEEE Trans. Ultrason. Ferroelectr. Freq. Control* **66** 772
[38] Marmonier M, Robert S, Laurent J and Prada C 2022 *Ultrasonics* **124** 106708
[39] Lin S C and Li P C 2023 *IEEE Trans. Ultrason. Ferroelectr. Freq. Control* **71** 85
[40] Li M, Liang S and Lu M 2024 *Phys. Med. Biol.* **69** 185008
[41] Liu J, Jiang C, Liu C, Xu K and Ta D *Chin. Phys. B* (Submitted)
[42] Guan H, Jiang C, Xu K and Ta D 2025 *Ultrasonics* **158** 107809
[43] Wang P, Ma H, Liu T, Liu C, Li D and Ta D 2025 *Chin. Phys. B* **34** 044301
[44] Rodriguez-Molares A, Rindal O M H, D'hooge J, Måsøy S E, Austeng A, Bell M A L and Torp H 2019 *IEEE Trans. Ultrason. Ferroelectr. Freq. Control* **67** 745
[45] Zhao J J, Jin S M, Wang Y K, Wang Y and Peng Y H 2025 *Chin. Phys. B* **34** 084301